ISSN 0915-633X

NATIONAL INSTITUTE FOR FUSION SCIENCE

Collisionless Magnetic Reconnection Associated with Coalescence of Flux Bundles

M. Tanaka

(Received - Oct. 18, 1994)

NIFS-315 Nov. 1994

RESEARCH REPORT
NIFS Series

NAGOYA, JAPAN

Collisionless Magnetic Reconnection Associated with Coalescence of Flux Bundles

Motohiko Tanaka

National Institute for Fusion Science

Nagoya 464-01, Japan

Abstract

The basic process of collisionless reconnection is studied in terms of coalescence of magnetized flux bundles using an implicit particle simulation of two-dimensions. The toroidal electric field that directly relates to magnetic reconnection is generated solenoidally in a region much broader than the current sheet whose width is a few electron skin depths. The reconnected flux increases linearly in time, but it is insensitive to finite Larmor radii of the ions in this Sweet-Parker regime. The toroidal electric field is controlled by a balance of transit acceleration of finite-mass electrons and their removal by sub-Alfvenic $E \times B$ drift outflow. The simulation results supports the collisionless Ohm's law $E_t \cong \eta_{eq} J_t$ with η_{eq} the inertia resistivity.

Keywords: magnetic reconnection, collisionless dissipation,
electron inertia, implicit particle simulation.

I. Introduction

Magnetic reconnection plays a significant role in changing topology of magnetic field and converting magnetically stored energy to plasma flow and thermal energies in fusion and astrophysical plasmas[1–3]. The global study of magnetic reconnection commonly relies on the MHD (magnetohydrodynamic) equations and the Ohm's law which include ad hoc dissipation of plasma current[4,5]. However, an origin of anomalous dissipation in high-temperature plasmas that should arise from non-Coulomb collisions has remained a key question of magnetic reconnection for many years.

For the origin of anomalous dissipation, a variety of mechanisms were proposed such as wave-particle interactions associated with microinstabilities, chaotic orbits of plasma particles, and finite inertia of the electrons. The lower-hybrid-drift instability[6,7] was once considered most promising for giving rise to anomalous resistivity in fusion and magnetospheric environments until its absence was proved at the magnetic null point due to high plasma beta. Recently, particle orbits were numerically followed to calculate the electrical conductivity for a configuration modelling the earth's magnetospheric neutral sheet[8].

An importance of electron inertia for collisionless reconnection was first noticed in the MHD framework[9], and then its kinetic effect was studied assuming the electromagnetic fields pertinent to magnetic reconnection[10]. Later studies focused on the collisionless process of m=1 tearing mode invoked by the experimental observations of fast sawtooth crash. In these studies, the MHD fluid equations and the generalized Ohm's law with electron inertia current, $E_{\|} = \eta J_{\|} + (4\pi/\omega_{pe}^2) dJ_{\|}/dt$, were adopted[11–16]. With weak dissipation $\eta J_{\|}$, the toroidal current was generated in a thin dissipation region whose spatial scale was much less than the electron skin depth; the "reconnection" electric field vanished at its center, $E_{\|} \cong dJ_{\|}/dt \rightarrow 0$, and therefore, non-zero resistivity was required to split and reconnect the magnetic field.

Nonlinear growth of magnetic island was investigated for resistive plasmas of plain geometry[17–19] and for the collisionless m=1 tearing mode[14–16] which provides another case of magnetic reconnection. Particle simulations were also performed[20,21]. However, the basic issues of magnetic reconnection, especially the formation and structure of the toroidal electric field and the dissipation region, have not been well clarified because of the nature of the MHD equations or the choice of simulation parameters. Precisely, the fluid MHD simulations including the electron inertia[12,14,15] produced contradictory results depending on their adopted equations.

As an alternative approach of elucidating the basic process of collisionless reconnection[22] without assuming the Ohm's law, we study here a coalescence process of two flux bundles by means of the $2\frac{1}{2}$-D (two space dimensions, three velocity components) electromagnetic, implicit particle simulation method[23] (macro-particle code "HIDEN"). The process follows the coalescence instability which is caused by magnetic attraction between the same-directional currents, and is a fast process occurring in a few poloidal Alfven times. In this paper, we limit the study to a magnetized plasma with the external toroidal magnetic field, as is often the case with high-temperature, non-resistive plasmas found in magnetic fusion devices[24,25] and the solar corona[26].

It is remarked that the coalescence process leads to magnetic reconnection without externally applying the electric field, $E_t^{(0)} = 0$, and that compressibility is ignorable due to the ambient magnetic field. These features will simplify the physical process of collisionless reconnection and enable us easily to identify the reconnection electric field.

Concerning the methodology, an advantage of the implicit particle simulation[23,27] over the conventional electromagnetic particle-in-cell simulation is realization of large time-and-space scales while including electron dynamics, i.e., $L \geq c/\omega_{pe}$ and $\omega_{pe}\tau \gg 1$, where c is the speed of light and ω_{pe} is the electron plasma frequency. It has been

proved analytically and numerically that the wave-particle resonances, complicated particle orbit effects and the electrostatic shielding due to parallel electron motions are naturally incorporated in the implicit particle simulation. Moreover, it removes intense artificial particle collisions associated with high-frequency electromagnetic and Langmuir oscillations which are inevitable in the conventional particle codes.

The present simulation algorithm[23] solves the complete Maxwell equations for the electromagnetic field,

$$\partial \mathbf{E}/\partial t = c\nabla \times \mathbf{B} - 4\pi \mathbf{J}, \quad \nabla \cdot \mathbf{E} = 4\pi\rho, \tag{1}$$

$$\partial \mathbf{B}/\partial t = -c\nabla \times \mathbf{E}, \quad \nabla \cdot \mathbf{B} = 0, \tag{2}$$

where $\mathbf{E}$ and $\mathbf{B}$ are the electric and magnetic fields, respectively, and $\mathbf{J}$ and ρ are the current and charge densities. The Newton-Lorentz equations of motion without a collisional drag,

$$d\mathbf{x}_j/dt = \mathbf{v}_j, \tag{3}$$

$$d\mathbf{v}_j/dt = (e_j/m_j)[\mathbf{E} + (\mathbf{v}_j/c) \times \mathbf{B}], \tag{4}$$

are integrated in time for the new position $\mathbf{x}_j$ and velocity $\mathbf{v}_j$ of each particle, where e_j and m_j are the electric charge and mass of the j-th particle. When the electrons are magnetized in the entire plasma region, we can optionally use the drift-kinetic equations for the electrons,

$$d\mathbf{x}_j/dt = [v_{\|j}\mathbf{b} + \mathbf{v}_{\perp j}], \tag{5}$$

$$dv_{\|j}/dt = (-e/m_e)E_{\|} - (\mu_j/m_e)\nabla_{\|}B, \tag{6}$$

where $v_{\|j}$, $\mathbf{v}_{\perp j}$ are the parallel and perpendicular (guiding-center) velocities, respectively, $\mathbf{b}$ is the unit vector along the magnetic field, and μ_j is the magnetic moment. To solve Eqs.(1)-(6) [or Eqs.(1)-(4)] under large time-and-space scales, the time-decentering technique is used; it filters out high-frequency components of the

electromagnetic oscillations for which $\omega\Delta t \geq O(1)$, where ω is their characteristic frequency and Δt is a time step.

For actual solution of the electromagnetic field, Eq.(1) and (2) are combined to obtain the pseudo-elliptic equation to determine the future electric field under a large time step. The magnetic field is then calculated by Eq.(2). In Eq.(1), $\mathbf{J}$ and ρ are collected from the plasma particles by

$$\begin{aligned} \mathbf{J}(\mathbf{x}) &= \sum_j e_j \mathbf{v}_j S(\mathbf{x}-\mathbf{x}_j), \\ \rho(\mathbf{x}) &= \sum_j e_j S(\mathbf{x}-\mathbf{x}_j), \end{aligned} \tag{7}$$

where $S(\mathbf{x})$ is an assignment function satisfying $\int S(\mathbf{x})d\mathbf{x} = 1$. All the plasma particles are advanced by Eqs.(3)-(6) [or Eqs.(3), (4)] using the electromagnetic field already obtained by Eqs.(1) and (2).

In order to have a good spatial resolution of the "dissipation region" which is characterized by a peaked toroidal current J_y to be formed around $x \cong \frac{1}{2}L_x$, spatially-fixed uneven meshes are adopted in the x-direction. Furthermore, to keep the particle fluctuations in a low level, one giant particle is split into a few small particles with the (e_j/m_j) ratio fixed when it has entered the fine-mesh region located around the center of the system. On the other hand, small particles once split are not coalesced to the original size to avoid physics ambiguities.

The organization of the paper will be the following. Sec.II will describe the particle simulation results of the coalescence of two flux bundles under the ambient toroidal magnetic field. The mechanism of collisionless reconnection will be stated in Sec.III. Discussions on the electric field and collisionless dissipation will be made in Sec.IV. Finally, Sec.V will give a brief summary and future prospects of the study.

II. Particle Simulation Results

A series of runs has been performed to study the basic process of collisionless reconnection. In this section, the simulation condition, parameters and results of the standard run - Run A, will be described unless otherwise specified.

A charge-neutral, homogeneous plasma is initialized with the same number of ions and electrons (64 ions/cell) in a doubly-periodic Cartesian system of the two-dimensions. The system size is $L_x = 400c/\omega_{pe}$ and $L_z = 300c/\omega_{pe}$ with 320×72 cells. The grid interval is $\Delta x \cong 0.55c/\omega_{pe}$ for the central part (107 cells) and $\Delta x \cong 1.6c/\omega_{pe}$ for the rest of the system, and $\Delta z \cong 4.1c/\omega_{pe}$ in the z-direction. Three components of the particle velocity are generated according to the Boltzmann distribution of given temperatures.

The ions residing in two square areas are given initial drift $V_{di}/c = 0.01$ toward the positive y-direction which produces a pair of flux bundles. All the electrons drift initially at an equal velocity in the y-direction so that the plasma system has no net dc-current. (The initial flux bundle current is sustained by the ions since it makes easier to observe the return current due to the electrons. When the initial current is assigned to the electrons, the results essentially stay the same.) The physical parameters are the mass ratio $m_i/m_e = 100$, the strength of the external toroidal (y-direction) magnetic field $\omega_{ce}^{(0)}/\omega_{pe} = 1$, electron beta value $\beta_e = 8\pi n T_e/B^2 = 0.04$, and the temperature ratio $T_i/T_e = 1$. The Larmor radius of thermal ions becomes $\rho_i \cong 2c/\omega_{pe}$, and the time step is chosen to be $\omega_{pe}\Delta t = 50$.

Figure 1 shows the poloidal magnetic flux function Ψ defined by $\mathbf{B}_p = \nabla \times (\Psi \hat{y})$, and the toroidal component of the ion current $J_y^{(i)}$ for $t/\tau_A = 0$, 1.6 and 3.1. Here, the poloidal Alfven time is defined by $\tau_A = \frac{1}{2} d/v_{Ap} \sim 3200\omega_{pe}^{-1}$, where $d = 160c/\omega_{pe}$ is the initial separation of the two flux bundle centers, and $v_{Ap} = B_p^{(0)}/(4\pi m_i n)^{1/2} \sim 0.025c$ is the "poloidal" Alfven speed. In the simulation, the flux bundles with the same-

directional currents attract each other by magnetic force, and they get flatly squeezed at the contact surface before magnetic reconnection sets in, as shown in Fig.1(b). The formation of the elongated (Y-shaped) dissipation region is in common with merging of mildly peaked islands simulated with resistive MHD equations[17–19]. Occurrence of magnetic reconnection is roughly identified by measuring the amount of isolated poloidal magnetic flux which is contained in either of the flux bundles. The number of the isolated Ψ-contours does not change for Fig.1(a) and (b), but it decreases between (b) and (c). (The total poloidal magnetic flux is conserved within three percent.)

The toroidal current of the ions shown in the lower panels of Fig.1 gradually pinches off and its contours become more or less round-shaped in an early time because the initial plasma pressure is uniform. As the two flux bundles approach, a substantial amount of "negative" toroidal current is generated to fill in the narrow channel dividing the flux bundles (the dashed contours correspond to negative values). By this time, the channel width has been narrowed to the size comparable to electron skin depth, $L_B \cong 3c/\omega_{pe}$ (half-width). This negative current is carried mostly by the electrons, $|J_y^{(e)}/J_y^{(i)}| \sim 5$, which reaches a maximum around $t \cong 1.8\tau_A$. The intensity and area of the current sheet decrease gradually as the coalescence proceeds in the saturation stage. It is remarked that, since the negative current in the current sheet provides a repulsive force against the flux bundles with the positive current, it needs to be diminished to have steady reconnection.

The time histories of the toroidal current J_y and the electric field E_y measured in a small region at $x \cong \frac{1}{2}L_x$ are shown in Fig.2 in logarithmic scales (the signs reversed). In the early phase up to $t \cong 2\tau_A$, the toroidal electric field E_y is observed to grow roughly exponentially with an amplitude oscillation arising from the initial loading. The sign of the E_y field at $x \cong \frac{1}{2}L_x$ stays the same during the whole simulation period, $E_y < 0$. This electric field, which directly relates to magnetic reconnection through the Faraday's law

Eq.(2), is purely electromagnetic (solenoidal), since a charge separation does not occur in the y-direction ($\partial\varphi/\partial y = 0$ with φ the electrostatic potential). Also, the toroidal current at the x-point increases exponentially in the same growth rate as that of the E_y field, $\gamma\tau_A \sim 2.6$. The growth phase of these x-point quantities is succeeded at $t \cong 2\tau_A$ by a steady phase with $\partial E_y/\partial t \cong 0$ and the finite-amplitude toroidal electric field, $E_y \neq 0$. Furthermore, in the steady phase we see the proportionality relation $E_y \propto J_y$ at the x-point.

In the lower panel of Fig.2, the time history of the isolated poloidal magnetic flux is shown in a linear scale. The isolated flux $\Delta\Psi$ is defined as the difference in the flux values at the peak of the flux bundle (averaged) and the separatrix. The isolated flux stays nearly in the same level in the early growth phase up to $t/\tau_A \cong 1.8$. Then, it turns into a time-linear decrease phase which corresponds to the steady phase of the toroidal electric field. However, the flux reconnection does not proceed until $\Delta\Psi \sim 0$ but slows down for $t/\tau_A \geq 4$; approximately a third of the initially isolated flux remains unreconnected. This incomplete reconnection happens because the two magnetic field lines contacting vertically across the x-line becomes nearly parallel; this appears to be similar to the partial reconnection experiment of two co-helicity flux cores[28] (though the experiment is semi-collisional). The observed time-linear annihilation of the isolated magnetic flux, which is the Sweet-Parker type reconnection[29,30], is consistent with nearly constant value of the toroidal electric field, as observed in Fig.2.

Here, it is noted that, for the present magnetic profile, the nonlinear growth phase identified in the resistive MHD studies[17,19] is almost absent, and that the full-nonlinear stage with linear flux annihilation starts shortly following the onset of magnetic reconnection. This differs from the m=1 tearing mode[14–16] whose eigenmode structure is different ($\Delta' \gg 0$).

The two-dimensional snapshots of the electric and magnetic fields, and the toroidal

currents of the ions and electrons for $t/\tau_A = 1.6$ are shown in Fig.3. We note that magnetic reconnection has not started at this time. The toroidal component of the electric field E_y in panel (b) takes a positive value in the regions corresponding to the interior of the flux bundles, whereas it becomes negative in a broad region sandwiched by them. The half-width of the $E_y < 0$ layer measured at $z = \frac{1}{2}L_z$ is $L_E \sim 45c/\omega_{pe}$. The spatial extent of the induced toroidal "current sheet" in Figs.3(d)(e), which characterizes the dissipation region, is much narrower than the $E_y < 0$ region.

It is remarkable that, before the onset of magnetic reconnection, the toroidal electric field E_y is small on the x-line compared with the surrounding area, as seen in Fig.3(b), because the E_y field first grows in the regions apart from the x-line. Thus, the magnetic flux does not merge but piles up on the both sides of the x-line. This fact was reflected on the squeezed contours of the poloidal flux function in Fig.1(b). Meanwhile, with the exponential growth of the toroidal electric field observed in Fig.2, the x-line turns into the global minimum of the E_y field and magnetic reconnection starts. This time sequence is quite consistent with the magnetic flux reconnection at the x-point.

The poloidal component of the electric field displayed in Fig.3(a) is more intense than its toroidal component. This electric field is stationary in time and has a divergence, which is better depicted in the electrostatic potential φ of Fig.3(f) such that $\mathbf{E}_p = -\nabla\varphi$. Obviously, the charge redistribution has occurred in a quadrupole configuration in the regions surrounding the x-point; more negative charge accumulates in the first and third quadrants with the origin at the x-point.

Fig.4 gives an idea how the toroidal electric field arises during the growth phase of collisionless reconnection. Panel (a) shows the y-component of the curl of the magnetic field, $c(\nabla \times \mathbf{B})_y$. This should be close to the toroidal current. This quantity is positive valued inside the flux bundles and is negative valued between them. The quantity that equals to the displacement current, $c(\nabla \times \mathbf{B})_y - 4\pi J_y$ (time-averaged), is shown

in panel (b). We find that the peaks inside the flux bundles in panel (a) are almost equalized by the current J_y in panel (b), but its cancellation is not complete in a broad area expanding between the flux bundles. This area coincides with that of the negative E_y field already shown in Fig.3(b).

The "parallel" electric field in the plasma is shown in Fig.5. We define at each point the parallel electric field by $E_{\parallel} = E_y b_y - \mathbf{b} \cdot \nabla \varphi$, where $\mathbf{b}$ is the unit vector along the helical magnetic field. In panel (b), the projection of the poloidal electric field onto the magnetic field, $(-\mathbf{b} \cdot \nabla \varphi)$ is shown, and in panel (c) that of the toroidal electric field, $E_y b_y$. The sum of the fields in (b) and (c) is seen to be almost cancelled, $E_{\parallel} \cong 0$, everywhere except in the vicinity of the dissipation region. One conclusion is that the electrostatic potential in the quadrupole form is a result of the electrostatic shielding by electron adjustment.

The above observations in Fig.4 and 5 reveal a chain such that the toroidal electric field is generated in response to the magnetic attraction which drives the coalescence. Namely, the toroidal current develops under the influence of the magnetic force and the parallel electric field. This alters the poloidal magnetic field by Ampere's law, which immediately results in the the toroidal electric field. It's non-shielded component then accelerates the plasma and produces the toroidal current, which closes the chain. Also from the aforementioned observations, we can identify three regions with (i) $J_y < 0$ (current sheet), (ii) $E_{\parallel} < 0$ (non-shielded region), and (iii) $E_y < 0$. The regions (i) and (ii) almost overlap, but the region (iii) is much broader. This multi scale-length for the toroidal current and the electric field is a different feature from the prediction of the MHD theory.

The electrostatic potential thus generated leads to both the E_z field laterally across the flux bundles in Fig.3(a), and a more intense electric field E_x concentrated in the dissipation region. Since the width of the layer l_x is less than its length l_z, we have

$E_x/E_z \cong l_z/l_x \sim 3$. On the other hand, the non-shielded electric field $E_{\|}$ accelerates the light mass electrons and produces the observed toroidal current confined in the vicinity of the x-line. The non-shielded parallel electric field $E_{\|}$ may be attributed to that the magnetic field is perpendicular to the x-z plane, and that $E_p \cong 0$ due to symmetry in φ.

The poloidal components of the ion and electron currents, the electric and magnetic fields in the central region are shown in Fig.6. The ion flow velocity is almost the same with that of the current as the plasma density is nearly uniform due to incompressibility. The ions stream vertically almost along the equicontour of the potential φ toward the dissipation region and are ejected laterally within the fans stretching from the x-point. The inflow speed v_{in} corresponds to $\frac{1}{2}d/v_{in} \sim 3\tau_A$, which is close to the growth time in Fig.2. The flow pattern in panel (a) and the electric field in panel (c) are quite well superimposed. In addition, the observed outward velocity $V_z = 0.021c$ ($\sim v_{Ap}$) coincides with $V_{E\times B} \sim 0.022c$ estimated by the poloidal electric field E_p. These facts reveal that the plasma flow is sustained by the $E_p \times B$ drift.

Although both the toroidal and poloidal electric fields contribute to the plasma convection, the poloidal electric field is predominant, $\mathbf{E} \times \mathbf{B} \cong \mathbf{E}_p \times \mathbf{B}_t$ as $E_p \gg E_t$ and $B_t > B_p$. Since $E_x > E_z$, the outflow velocity is faster than the inflow speed into the dissipation region. The electron current in Fig.6(b) nearly cancels that of the ions in the present case for a magnetized plasma. A slight asymmetric pattern in the electron current, i.e. anti-parallel current wedges penetrating through the dissipation region, is accounted for by the ∇B drift.

An infinite growth of the toroidal current in the dissipation region would repel the flux bundles with the opposite-sign current and impede magnetic reconnection. On the other hand, there is a clue which tells that the observed high-speed outflow in the poloidal plane, by which the J_y current is carried, is removing the toroidal current off

the dissipation region and maintaining the steady reconnection.

In order to prove the last statement, a special run - Run B, has been designed where the poloidal electric field (E_x, E_z) is artificially reduced to 70% of its real value within the central rectangular area, $x \in \frac{1}{2}L_x \pm 10c/\omega_{pe}$, $z \in (\frac{1}{2} \pm \frac{1}{4})L_z$. The other conditions are being fixed. The plots of the poloidal flux function show that the flux bundles are sliding clockwise around the x-point, and that the formed x-line is inclined with respect to the z-axis. The plasma density piles up in the dissipation region, and the poloidal outflow of the ions and electrons become quite distorted for $t > 2\tau_A$. Quantitatively, the toroidal electric field at the x-point grows exponentially in Fig.7 but only to a lower saturation level compared to Fig.2. The isolated flux first begins to merge linearly in time, but soon it slows down for $t > 2.5\tau_A$. The reconnection rate for Run B is drastically reduced from $(d\Delta\Psi/dt)/\Delta\Psi^{(0)} \sim -0.23\tau_A^{-1}$ of Run A to $-0.06\tau_A^{-1}$. Thus, it is concluded that steady removal of the toroidal current by poloidal plasma outflow controls the toroidal electric field at the x-point.

The growth of the toroidal electric field may be roughly scaled as, $(\partial E_y/c\partial t)/(\nabla \times B_p)_y \sim (v_{Ap}/c)^2$ in the growth phase, as will be discussed in Sec.IV. For the parameters of Run A, we have $(v_{Ap}/c)^2 \sim 5 \times 10^{-4}$. On the other hand, the observation of the electric field in Fig.2 yields 1.4×10^{-4} for the above ratio. The agreement between the theoretical scaling and the observation is reasonable.

Another run - Run C, has been performed with the initial drift speed reduced to a half that of Run A, $V_{di}/c = 5 \times 10^{-3}$. The Alfven speed for this run also becomes a half. The growth speed of the toroidal electric field, $(\partial E_y/c\partial t)/(\nabla \times B_p)_y$, is estimated to become one quarter compared to Run A. The time histories of the toroidal electric field E_y and the current J_y measured at the x-point are shown in Fig.8. If the amplitudes of E_y and J_y are reduced to a quarter of their counterparts and the time axis is normalized by the new Alfven time, these plots will be almost the same with those in Fig.2. The

time history of the isolated flux will also be similar if the $\Delta\Psi$ axis is reduced to a half. Therefore, the growth of the toroidal electric field is concluded to follow the theoretical scaling Eq.(10), which supports physical validity of the simulations.

Here, let us look at two complementary runs to Run A that use either half the grid points in the x-direction or four times more number of particles. These runs are to check the spatial resolution or particle noise problems in the dissipation region. In the former run, the grid size at the center is $\Delta x \cong 1.1c/\omega_{pe}$, and in the latter run the particle density is 256 ions (and electrons) per cell. Despite of these changes, the overall results including the width of the dissipation region and the flux reconnection rate, $(d\Delta\Psi/dt)/\Delta\Psi^{(0)} \sim -0.27\tau_A^{-1}$, have stayed quite similar. If either the skin effect, discretization inaccuracy or particle noise has anything to do, we should detect an appreciable difference in the electric field E_y and the above quantities. Thus, it seems unlikely that the spatial resolution and the particle noise are affecting the aforementioned simulations of collisionless reconnection (except for a hyper-fine structure below c/ω_{pe} scales if there is).

It is emphasized that another series of the particle simulations by the HIDEN code has reproduced the dependence of the reconnection rate on the initial magnetic profile[31]. When the force-free equilibrium by Fadeev et al.[32] is adopted as the initial condition, the reconnected magnetic flux increases linearly in time for the coalescence of mildly peaked islands with $\epsilon = 0.3$. By contrast, magnetic reconnection is observed to become faster and scale like $\Delta\Psi(0) - \Delta\Psi \sim t^2$ for highly peaked magnetic islands with $\epsilon = 0.7$, in good agreements with the MHD simulation[33].

Under these circumstances, a role of the ion Larmor radius effect in the coalescence process has been examined. A few other runs have been made so that the ion Larmor radius varies as $\rho_i/L_B \cong 0.2 \sim 2$, by changing either the mass ratio $m_i/m_e = 50 \sim 200$ or the ion temperature $T_i/T_e = \frac{1}{9} \sim 9$. However, no appreciable change has been

observed in the width of the dissipation region or the flux reconnection rate, which scatters in a range $(d\Delta\Psi/dt)/\Delta\Psi^{(0)} \sim -(0.23 \sim 0.27)\tau_A^{-1}$. Thus, it is concluded that collisionless reconnection in the Sweet-Parker regime, where the reconnected flux increases linearly in time, is governed by the electron dynamics.

III. Mechanism of Collisionless Reconnection

The simulation results described in Sec.II will let us to construct the following scenario of collisionless reconnection. Here, we should remember that the inertia and parallel pressure effects of the electrons, the electrostatic field effect (as well as Larmor radius effect of the ions) have been included through Eqs.(1)-(6). The process (i) precedes (ii) and (iii):

(i) In the growth phase, the toroidal electric field E_y is generated solenoidally in a broad area extending far beyond the dissipation region.

(ii) The steady phase with the finite-amplitude toroidal electric field, $E_y < 0$, succeeds the growth phase.

(iii) Magnetic reconnection proceeds in the presence of the toroidal electric field, $\partial \mathbf{B}_p/\partial t = -c\nabla \times (E_y \hat{y}) \neq 0$.

The toroidal electric field E_y is purely electromagnetic since a charge-separation in the y-direction does not occur in the two-dimensional geometry. A catalytic process in the phase (ii) is: the parallel electric field $E_\parallel \cong E_y$ produces the toroidal current J_y in the dissipation region, which gives rise to the proportionality relation, $E_y \propto J_y$. Outside, by contrast, the electrostatic potential φ, hence the poloidal electric field E_p, is generated by electron adjustment to shield the parallel electric field,

$$E_\parallel \;=\; E_y b_y - \mathbf{b}\cdot\nabla\varphi \;\cong 0. \tag{8}$$

This poloidal electric field generates, in turn, the sub-Alfvenic $E_p \times B$ plasma outflow. Since the plasma particles carry the current with their motion, this poloidal outflow

results in a rapid removal of the toroidal current off the dissipation region. On the other hand, the parallel streaming along the magnetic field has turned out to take a less role in their removal than the $E_p \times B$ flow. This removal of the toroidal current maintains the steady toroidal electric field in the phase (ii) (cf. Run B). A fast process in ω_{pe}^{-1} time scale is transiently involved which acts to inhibit over-reaction of the plasma and maintain, $\partial E_y/\partial t = c(\nabla \times B_p)_y - 4\pi J_y \cong 0$. Actually, $\partial E_y/\partial t$ slightly deviates from zero in such a way to be consistent with the E_y field growth.

IV. Discussions

The macro-particle simulations have produced the basic results that agree with the previous MHD simulations[17,19], such as formation of the elongated dissipation region and the time-linear flux reconnection rate. On the other hand, the present particle simulations differ from the collisionless MHD studies in the following points:

(1) The toroidal electric field is generated in a region much broader than the current sheet (dissipation region), $L_E \gg L_B$.

(2) The width of the current sheet is a few times the electron skin depth, $L_B \sim 3c/\omega_{pe}$, and does not shrink to a smaller scale.

(3) The reconnection rate is insensitive to the Larmor radii of the ions for $\rho_i/L_B \leq O(1)$ in the Sweet-Parker regime.

The above differences are considered to arise from the kinetic approach, Eq.(1)-(6), instead of the MHD equations and the Ohm's law. As noted, these equations include the inertia and parallel pressure effects of the electrons and the electrostatic field effect. Thus, the spatial boundaries of the $E_{\parallel} < 0$ and $J_y < 0$ regions are naturally determined, instead through violation to the frozen-in condition via resistivity or the solution matching at the boundary points. A not very spiky current sheet listed in (2) seems reasonable, because the parallel electron streaming along the magnetic field is

expected to smoothen the spiky structure. Also because, from a "macro" viewpoint, the current saturation in the dissipation region limits the repulsive force between the sheet current and the flux bundles[34], which makes steady magnetic reconnection possible.

It has been observed in Fig.2 that the toroidal current and the electric field develop simultaneously at the x-point. As the magnetic field is almost toroidal there, the non-shielded E_y electric field can efficiently accelerate the plasma along the magnetic field to produce a large toroidal current. The low-frequency part of the toroidal electric field is treated by Eqs.(1),(2) neglecting the displacement current $\partial E_y/\partial t$,

$$\nabla^2 E_y \cong \left(\frac{4\pi}{c^2}\right)\frac{\partial J_{Ty}}{\partial t}, \tag{9}$$

with $\mathbf{J}_T$ a divergence-free part of the current $\mathbf{J}$, since the displacement current is a small quantity,

$$\frac{1}{c}\frac{\partial E_y}{\partial t}/(\nabla \times B_p)_y \sim (L/c\tau)(E_y/B_p) \sim (L/c\tau)^2, \tag{10}$$

where L is the width of the dissipation region and τ the growth time (cf. Eq.(14)). If we take $J_y(x,t) = J_0 e^{\gamma t}/\cosh^2(x/L)$ as observed in Sec.II, the electric field may be calculated to be,

$$E_y(x,t) \cong \left(\frac{4\pi\gamma}{c^2}\right) J_0 L^2 e^{\gamma t} \log\cosh(x/L) + F(t). \tag{11}$$

Although this argument is not self-consistent, it at least explains that, for the given current, the toroidal electric field also develops as $e^{\gamma t}$ in time with spatially extending beyond the current sheet.

A remaining question is why the displacement current which is ignored in Eq.(9) can keep the fixed sign in the growth phase such that,

$$\partial E_y/\partial t = c(\nabla \times \mathbf{B})_y - 4\pi J_y < 0. \tag{12}$$

Concerning this point, it is estimated that the response to the toroidal electric field is amplified to $(\omega_{pe}\tau)^2$ times by the plasma compared to via the displacement current. By

putting $J_y \sim (ne^2/m_e)E_y\tau_{tr}$ and the transit time being close to the growth time $\tau_{tr} \sim \tau$ (Sec.III), the ratio of the plasma contribution to the displacement current becomes

$$\left(\frac{4\pi}{c^2}\right)\frac{\partial J_y}{\partial t} \Bigg/ \frac{1}{c^2}\frac{\partial^2 E_y}{\partial t^2} \sim (\omega_{pe}\tau)^2 \gg 1. \tag{13}$$

Also, we have the right sign; when the toroidal electric field is growing ($E_y < 0$ assumed), we have both $\partial E_y/\partial t < 0$ and $\partial J_y/\partial t < 0$ in Eq.(9), as J_y is directly produced by the E_y field. The $\partial E_y/\partial t$ and $4\pi J_y$ terms, both of which have the same sign, balance the $(\nabla \times B_p)_y$ term in Eq.(12). The above question has been thus answered.

It is remarked that, during the growth phase, acceleration of the plasma (electrons) exceeds removal of the plasma current in the dissipation region, as evidenced by Fig.2. The removal increases quickly and balances the acceleration to achieve the steady toroidal electric field and, hence, magnetic reconnection. The final value of the toroidal electric field is obtained as,

$$E_y \cong \int_0^\tau \left(\frac{\partial E_y}{\partial t}\right) dt \sim (L/c\tau)B_p, \tag{14}$$

since the displacement current keeps the same sign for the time τ. For the coalescence, $\tau \sim \tau_A = L/v_{Ap}$ as shown in Sec.II, and we have $(\partial E_y/c\partial t)/\nabla \times B_p \sim (v_{Ap}/c)^2$. This ratio that amounts to $(1-5) \times 10^{-4}$ has agreed well with the observations in Figs.2 and 8, which physically verify the present simulations.

It has been shown in Section II that collisionless reconnection is governed principally by the electrons. A coexistence of the toroidal electric field and current in the dissipation region observed in this study also supports that the equivalent dissipation in the MHD description is provided by transit acceleration of the "finite mass" electrons[10]. Since we have the net toroidal electric field left in the dissipation region, i.e., $E_{\|} \cong E_y$, the toroidal current may be approximated in the first order by

$$J_y^{(e)} = (-e)n\delta v_y^{(e)} \cong (ne^2/m_e)E_y\tau_{tr}. \tag{15}$$

Here, τ_{tr} is an electron transit time through the dissipation region which is close to the growth time (Sec.III). The transit time is determined mainly by the poloidal $E_p \times B$ drift speed, and may be affected by the thermal streaming along the magnetic field[35]. The proportionality between J_y and E_y in Eq.(15) agrees well with the observation in Fig.2. Eq.(15) is cast in the form of the collisionless Ohm's law,

$$E_y \cong \eta_{eq} J_y, \tag{16}$$

where the equivalent resistivity is defined by $\eta_{eq} = 4\pi/\omega_{pe}^2 \tau_{tr}$. Substitution of Eq.(16) into the Ampere's law yields the toroidal electric field, $E_y \cong (c\tau_{tr}/L_B)B_p/(1+\omega_{pe}^2\tau_{tr}^2)$, where $L_B = (\partial \log B_p/\partial x)^{-1}$. With the Faraday's law, we obtain the width of the dissipation region,

$$L_B^{(th)} \cong c/\omega_{pe}. \tag{17}$$

The same result was derived by the MHD equations and the Ohm's law with the electron inertia current[13]. Finally, with Eq.(16), the "equivalent" resistive time is obtained as $\tau_\eta = 4\pi L_B^2/c^2\eta_{eq} \sim \tau_{tr}$. The reconnection time is thus estimated to be

$$\tau_{rec} \sim (\tau_\eta \tau_A)^{1/2} \cong (2 \sim 3)\, \tau_A, \tag{18}$$

as the transit time is a few Alfven times. These values in Eqs.(17) and (18) account for the observed width of the current sheet and the reconnection time in Section II.

One of the most sophisticated issues of collisionless reconnection is how to remove the singularity at the x-point. The fluid inertia term behaves like $E_\parallel \sim \partial J_\parallel/\partial t + (\mathbf{v}\cdot\nabla)J_\parallel \to 0$ at the x-point. Thus, a small but finite resistivity $\eta J_\parallel \neq 0$ is required in the MHD theories[11–16] to reconnect magnetic field. In the particle simulation, by contrast, only few particles pass through this infinitesimally small x-point, and they escape this singularity either by random (non-symmetric) $\delta\mathbf{E}_\perp \times \mathbf{B}$ motion in the poloidal plane due to fluctuating $\delta\mathbf{E}_\perp$ field or micro-instabilities. Once off the x-point, the $E_p \times B$ and

∇B drifts carry the electrons steadily away, which means continuous removal of the toroidal current. The current saturation at the x-point will maintain the finite electric field, $E_y < 0$, and result in steady magnetic reconnection.

V. Summary and Concluding Remarks

In this paper, the basic process of collisionless magnetic reconnection was investigated using the electromagnetic, implicit particle simulation method (macro-particle code). As the two magnetic flux bundles coalesced, an elongated current sheet whose width is a few electron skin depths was formed between them. But, the current sheet did not collapse to a smaller scale, probably owing to parallel pressure effect of the electrons. The toroidal electric field that directly relates to magnetic reconnection was induced solenoidally in the early growth phase in the area much broader than the current sheet (dissipation region).

For the initial magnetic profile due to the square currents, the reconnected magnetic flux increased linearly in time. However, the reconnection rate was insensitive to the finite Larmor radii of the ions in this Sweet-Parker regime, even for $\rho_i > L_B$. It was mentioned, by contrast, that the reconnected flux increased quadratically for the highly-peaked initial profile. Since the present process follows the coalescence instability which is an ideal process occurring in a few poloidal Alfven times, its time development differs from the case with the m=1 tearing mode.

The sub-Alfvenic poloidal outflow was observed in the dissipation region. The poloidal electric field which is the result of electrostatic shielding of the parallel electric field acted as a catalyst of generating this $E_p \times B$ plasma flow in the magnetized plasma. Competition of transit electron acceleration due to the non-shielded toroidal electric field and their removal by the poloidal outflow was considered to control the toroidal current and, hence, the toroidal electric field at the x-point.

The present simulations showed primary dominance of the electron dynamics in the collisionless reconnection process. The aforementioned insensitivity to ion finite Larmor radius effect was consistent with this fact. The observed current and electric field supported that the equivalent resistivity in the MHD reconnection theory is provided by transit acceleration of the finite-mass electrons in the dissipation region. This yielded the collisionless Ohm's law $E_t \sim \eta_{eq} J_t$ with η_{eq} the inertia resistivity. Using this resistivity, the width of the dissipation region and the reconnection time were calculated to be an electron skin depth and a few Alfven times, respectively.

As the first concluding remarks, we refer to another series of coalescence simulations using the same initial geometry but without imposing the external magnetic field. Because of the magnetic-null in the plasma, the gyromotion of the electrons are traced using the Newton-Lorentz equations, Eqs.(3) and (4). The results show that, in contrast to the wide-spread poloidal current of the ions off the x-point, the electron current is quite concentrated to the narrow unmagnetized channel along the x-line. This remarkable difference in the current patterns produces a quadrupole structure in the toroidal magnetic field. On the other hand, the toroidal electric field E_y is generated in the early growth phase, as was described in this paper, and the isolated magnetic flux decreases linearly in time. The reconnection rate is again insensitive to the finite ion Larmor radius effect in the Sweet-Parker regime. Precise results are reported separately[36].

Finally, an investigation of the ion kinetic effects in non-Sweet-Parker regimes is currently undertaken. A three-dimensional study of collisionless magnetic reconnection is also an attractive and challenging problem. Although the present two-dimensional simulations which emulate a torus cross section ($\partial/\partial y = 0$) include most essential features of the collisionless reconnection, an addition of the third dimension may modify the process. Namely, a coupling of the toroidal current to the current-driven instabil-

ities may give rise to additional dissipation. Further, redistribution of the electrons along the magnetic field may affect the toroidal electric field and the reconnection rate. These issues await future particle simulations.

Acknowledgements

The author gratefully acknowledges valuable discussions with Dr.J.U.Brackbill and Dr.J.Todoroki on the ill-conditioned matrix inversion which occasionally appears in the solution of the coupled implicit equations in the HIDEN code. He thanks Dr.J.W.Van Dam for encouraging discussions.

References

1. J.W.Dungey, Phil.Magazine, 44, 725 (1953).
2. M.N.Rosenbluth, R.Y.Dagazian, and P.H.Rutherford, Phys.Fluids, 16, 1894 (1973).
3. B.B.Kadomtsev, Fiz.Plasmy, 1, 710 (1975) [Sov.J.Plasma Phys., 1, 389 (1975)].
4. W.Park, D.A.Monticello, and R.B.White, Phys.Fluids, 27, 137 (1984).
5. D.Biskamp, Phys.Fluids, 29, 1520 (1986).
6. R.C.Davidson and N.T.Gladd, Phys.Fluids, 18, 1327 (1975).
7. J.D.Huba, N.T.Gladd, K.Papadopoulos, J.Geophys.Res., 83, 5217 (1978).
8. W.Horton and T.Tajima, J.Geophys.Res., 96, 15811 (1991).
9. B.Coppi, Phys.Fluids, 8, 2273 (1965).
10. T.W.Speicer, Planet.Space Sci., 18, 613 (1970).
11. J.F.Drake, Phys.Fluids, 21, 1777 (1978).
12. J.F.Drake and R.G.Kleva, Phys.Rev.Lett., 66, 1458 (1991).
13. J.A.Wesson, Nucl.Fusion, 30, 2545 (1990).
14. A.Y.Aydemir, Phys.Fluids, B2, 2135 (1990).
15. M.Ottaviani and F.Porcelli, Phys.Rev.Lett., 71, 3802 (1993).
16. L.Zakharov, B.Rogers, and S.Miglioulo, Phys.Fluids, B5, 2498 (1993).
17. D.Biskamp and H.Welter, Phys.Rev.Lett., 44, 1069 (1980).
18. F.L.Waelbroeck, Phys.Fluids, B1, 2372 (1989).
19. X.Wang and A.Bhattacharjee, Phys.Fluids, B4, 1795 (1992).
20. T.Tajima, F.Brunel and J.Sakai, Astrophys.J., 258, L45 (1982).
21. D.W.Hewett, G.E.Francis and L.E.Max, Phys.Rev.Lett., 61, 893 (1988).
22. M.Tanaka, EOS Trans. (American Geophys. Union), 75, 263 (1994).
23. M.Tanaka, J.Comput.Phys., 107, 124 (1993); ibid., 79, 209 (1988).
24. K.McGuire and TFTR team, Phys.Fluids, B2, 1287 (1990).
25. B.Coppi, S.Migliuolo, F.Pegoraro and F.Porcelli, Phys.Fluids, B2, 927 (1990).

26. E.R.Priest, Solar Magnetohydrodynamics (D.Reidel Publ.Co., Holland, 1982).

27. H.X.Vu and J.U.Brackbill, Comput.Phys.Comm., 69, 253 (1992).

28. M.Yamada, Y.Ono, A.Hayakawa, M.Katsurai, and F.W.Perkins, Phys.Rev.Lett., 65, 721 (1990).

29. P.A.Sweet, Nuovo Cimento, 8, 188 (1958).

30. E.N.Parker, Astrophys.J.Suppl., 77, 177 (1963).

31. M.Tanaka, in "Theory of Fusion Plasmas" (edited by F.Troyon and E.Sindoni, Societa Italiana di Fisica, 1994).

32. V.M.Fadeev, I.F.Kvartshkhava, and N.N.Kamarov, Nucl.Fusion, 5, 202 (1965).

33. A.Bhattacharjee, F.Brunel, and T.Tajima, Phys.Fluids, 26, 3332 (1983).

34. M.Yamada, private communication (1994).

35. J.F.Drake and Y.C.Lee, Phys.Rev.Lett., 39, 453 (1977).

36. M.Tanaka, Comput.Phys.Comm., in press (1994).

Figure Captions

Figure 1. Snapshots of the poloidal magnetic flux function Ψ (top), and the y-component of the ion current $J_y^{(i)}$ (bottom) for the times $t/\tau_A =$ (a) 0, (b) 1.6 and (c) 3.1. The dashed contours correspond to negative values; $\Psi_{max} = 12.5$, $\Psi_{min} = -9.0$ for the upper panels, $J_t^{(i)} = 0.64$ for (a), and $J_t^{(i)} = 0.80$ for (b),(c) of the lower panels.

Figure 2. Time histories of the toroidal electric field (solid) and the toroidal current (dashed) in the upper panel, and the isolated poloidal flux $\Delta\Psi$ contained in either of the flux bundles in the lower panel; all of these quantities are measured in the vicinity of the x-point. (The signs of E_y and J_y are reversed.) The magnetic flux function is normalized as $e\Psi/m_e c^2$.

Figure 3. (a)(b) The poloidal and toroidal electric fields, respectively, (c) the poloidal magnetic field, (d)(e) the ion and electron toroidal currents, and (f) the electrostatic potential φ at time $t = 1.6\tau_A$. The maximum norms are (a) $E_p = 2.1 \times 10^{-2}$, (b) $E_t = 1.9 \times 10^{-3}$, (c) $B_p = 0.23$, (d) $J_t^{(i)} = 0.80$, (e) $J_t^{(e)} = 4.0$, and (f) $\varphi = 0.43$. (The electromagnetic fields are normalized as $eE/m_e c\omega_{pe}$.)

Figure 4. (a) The y-component of the curl of the poloidal magnetic field $c(\nabla \times B)_y$, and (b) the quantity that equals to the displacement current, $[c(\nabla \times B)_y - 4\pi J_y]$, which are averaged for the time centered at $t = 0.63\tau_A$.

Figure 5. (a) The parallel electric field $E_\parallel = E_y b_y - \mathbf{b} \cdot \nabla\varphi$, which is a sum of (b) projection of the poloidal electric field, $-\mathbf{b} \cdot \nabla\varphi$, and (c) that of the toroidal electric field, $E_y b_y$.

Figure 6. Enlarged plots of poloidal quantities in the vicinity of the x-point (vectors are plotted in every four x-grid points). The ion and electron currents for the time $t = 1.6\tau_A$ in (a) and (b), respectively, and the electric and magnetic fields in (c) and (d). The maximum norms of the vectors are, (a) $J_p^{(i)} = 1.4$, (b) $J_p^{(e)} = 1.4$, (c) $E_p = 2.2 \times 10^{-2}$, and (d) $B_p = 0.26$.

Figure 7. Time histories of the toroidal electric field (solid), the toroidal current (dashed), and the isolated poloidal flux $\Delta\Psi$ for Run B where the poloidal electric field (E_x, E_z) in the dissipation region is reduced to 70% of its real value.

Figure 8. Time histories of the toroidal electric field (solid), the toroidal current (dashed), and the isolated poloidal flux $\Delta\Psi$ for Run C with the initial drift reduced to a half compared to Run A, $V_{di}/c = 5 \times 10^{-3}$.

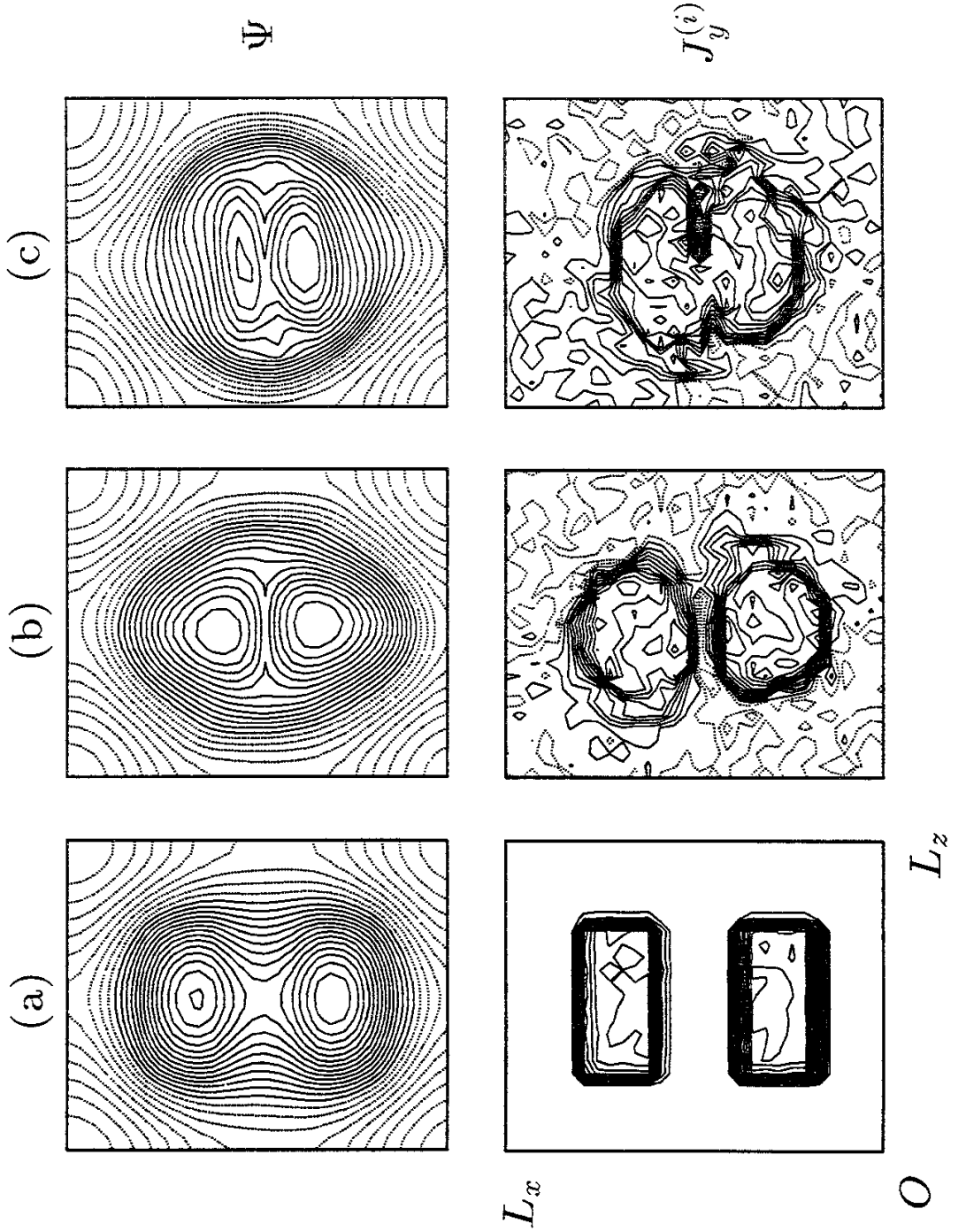

Figure 1.

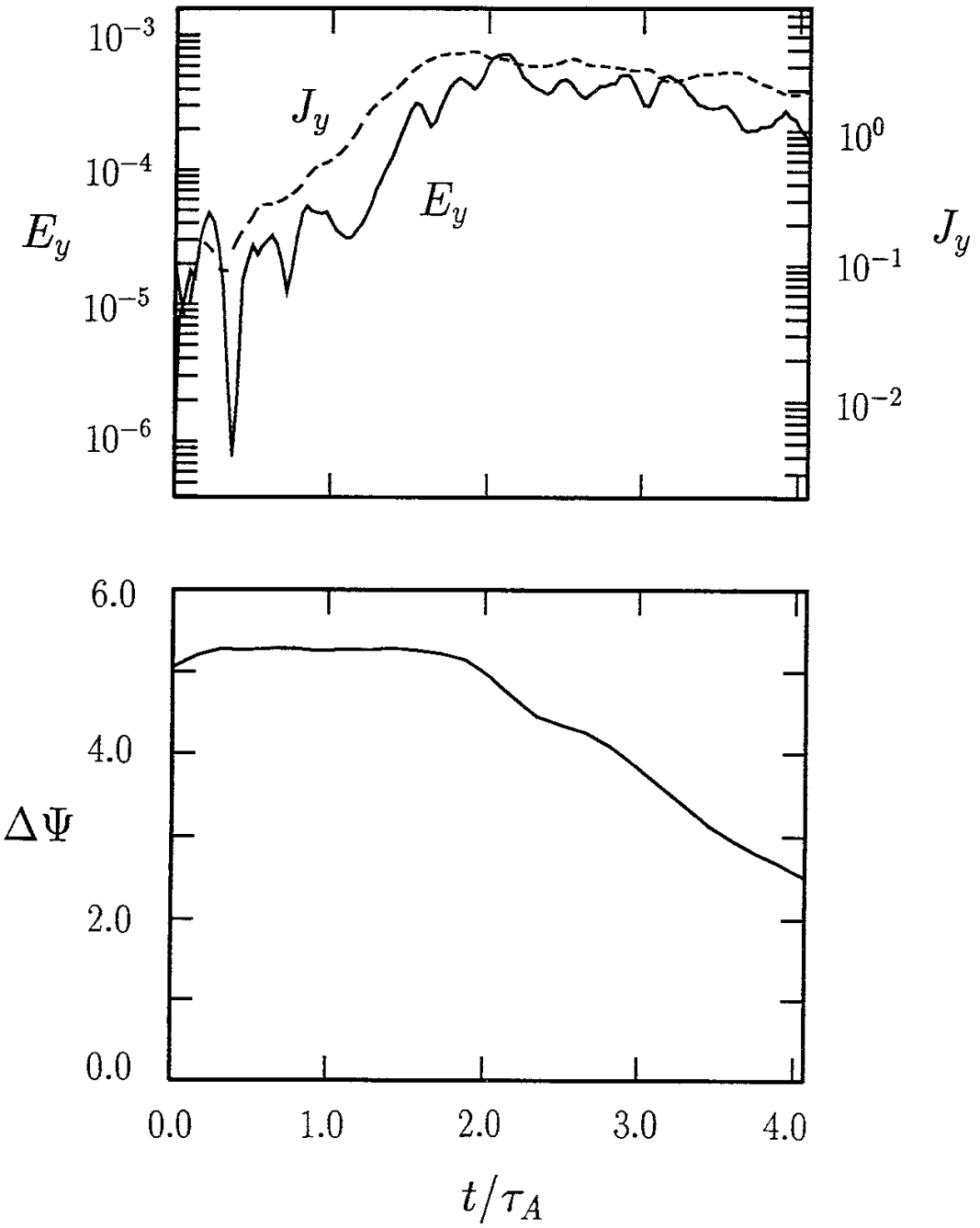
10^{-3}
10^{-4}
10^{-5}
10^{-6}
E_y
J_y
E_y
10^{0}
10^{-1}
10^{-2}
J_y
6.0
4.0
2.0
0.0
$\Delta\Psi$
0.0
1.0
2.0
3.0
4.0
t/τ_A

Figure 2.

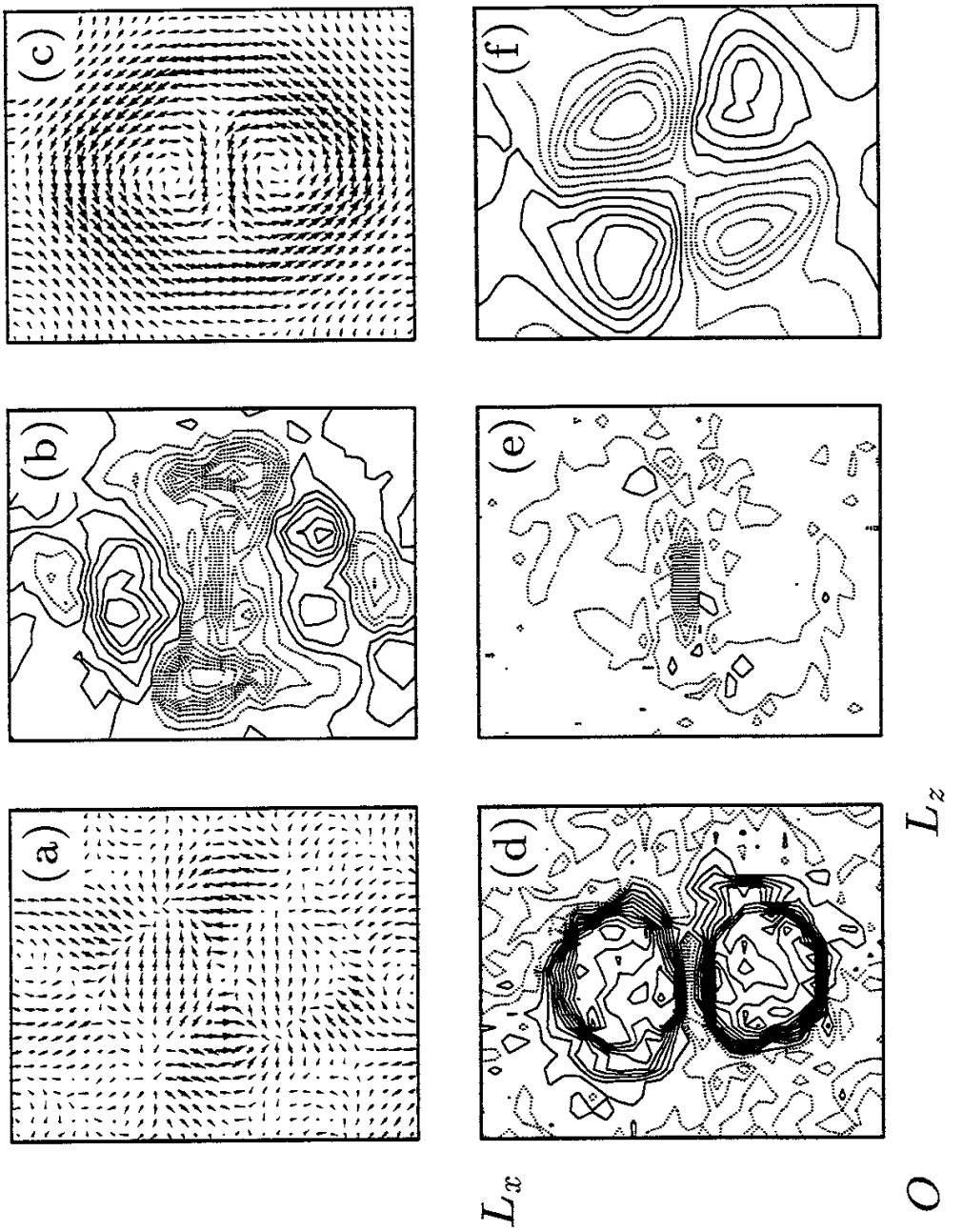

Figure 3.

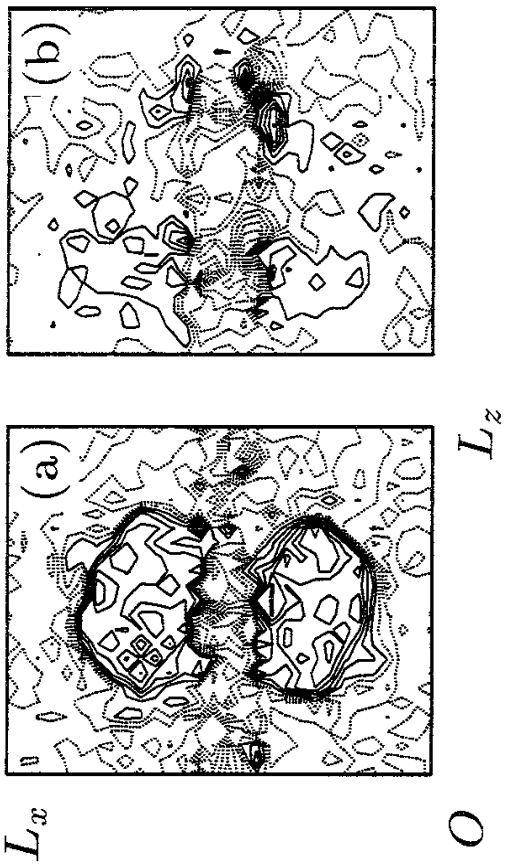

Figure 4.

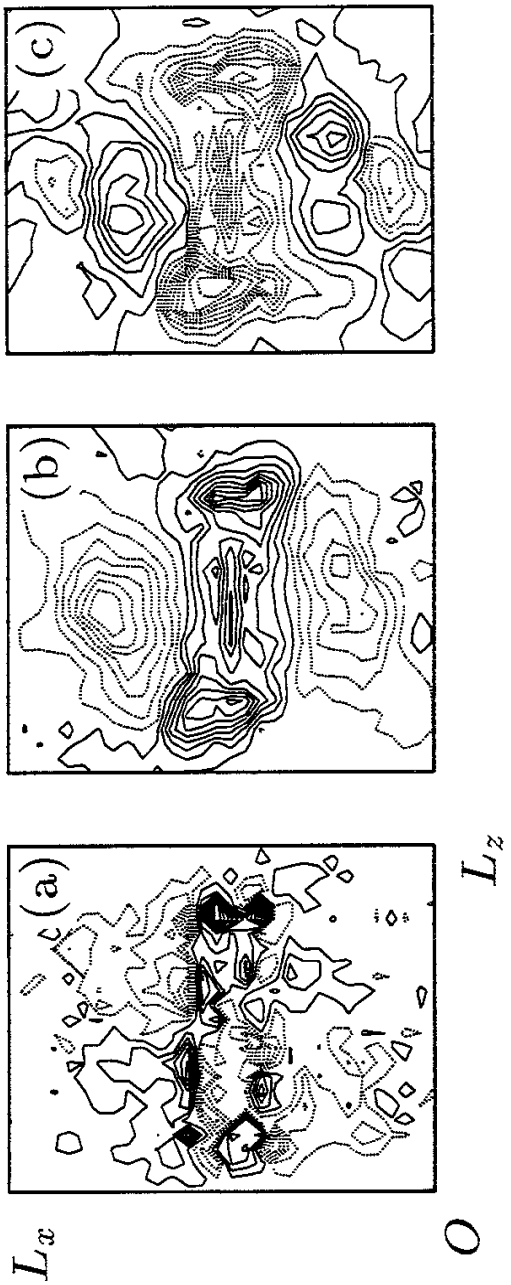

Figure 5.

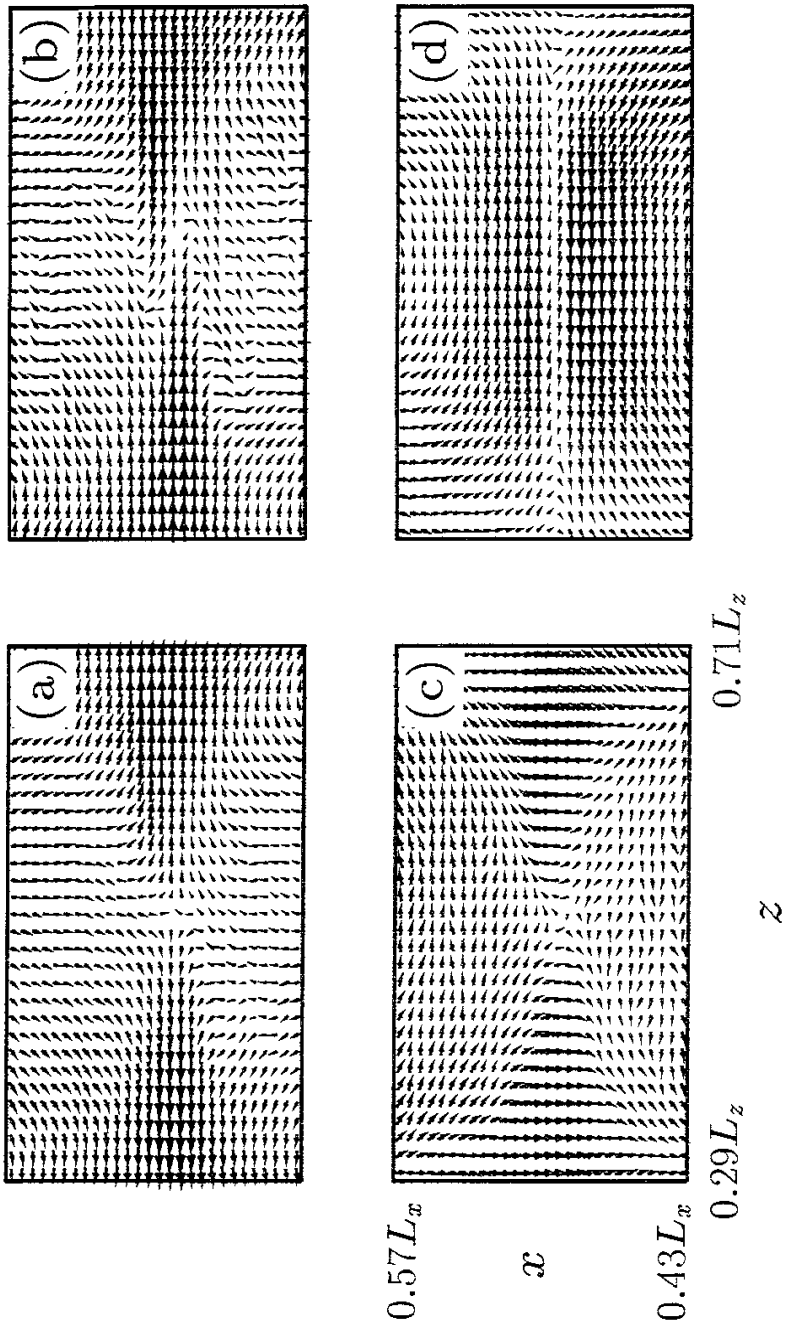

Figure 6.

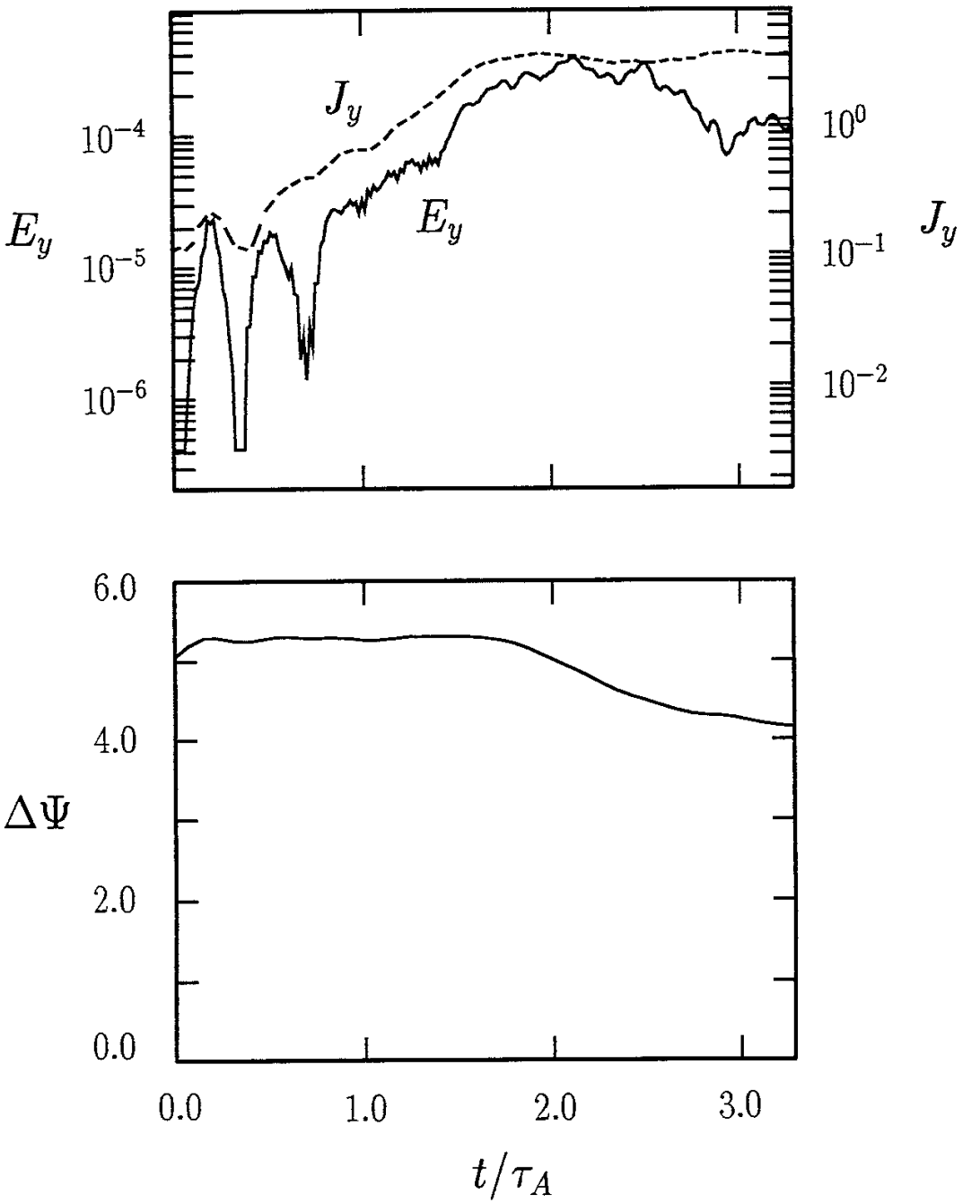
J_y
E_y
E_y
J_y
10^{-4}
10^{-5}
10^{-6}
10^{0}
10^{-1}
10^{-2}
6.0
4.0
2.0
0.0
$\Delta\Psi$
0.0
1.0
2.0
3.0
t/τ_A

Figure 7.

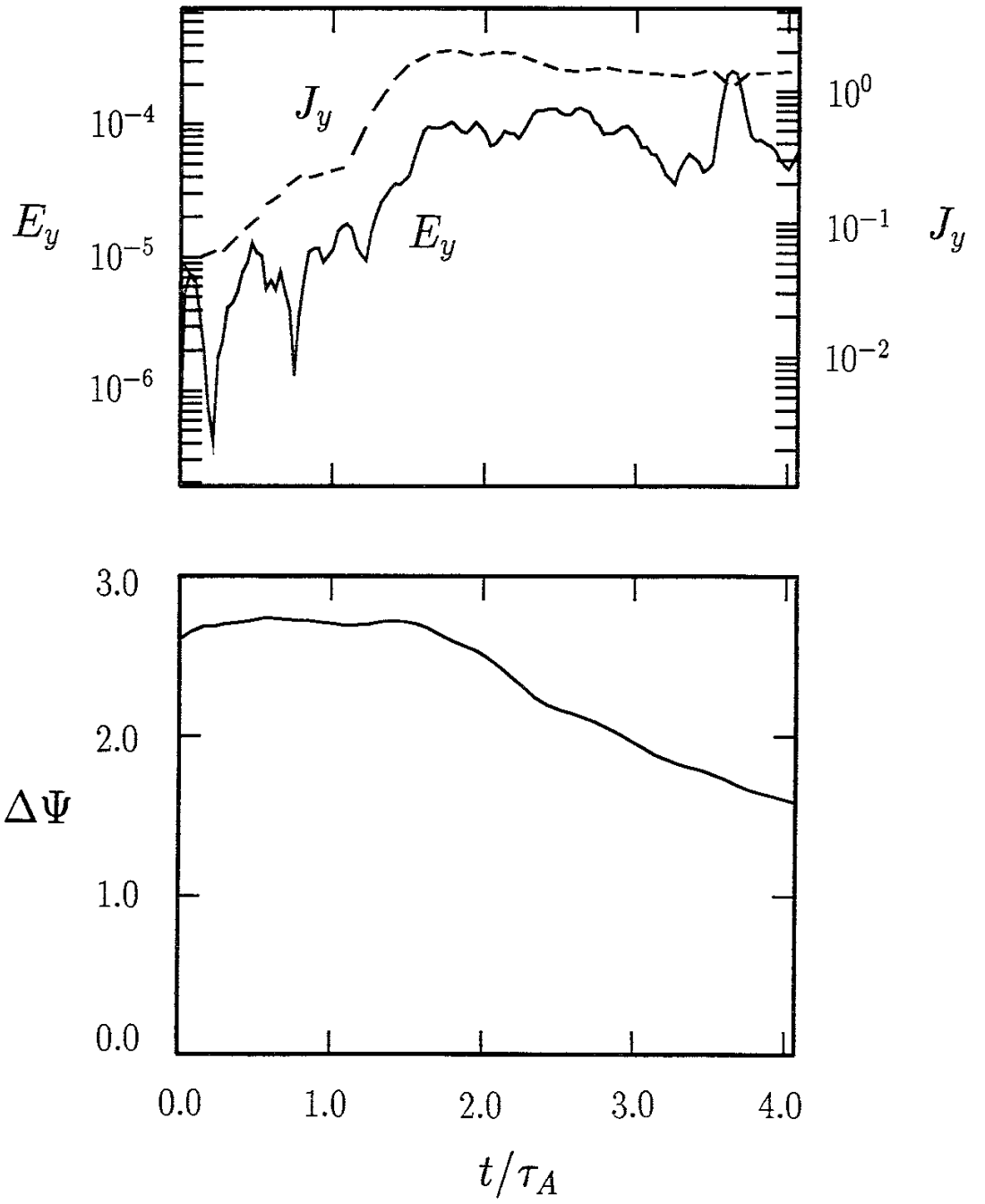
J_y
E_y
E_y
10^{-4}
10^{-5}
10^{-6}
10^{0}
10^{-1}
10^{-2}
J_y
3.0
2.0
1.0
0.0
$\Delta\Psi$
0.0
1.0
2.0
3.0
4.0
t/τ_A

Figure 8.

Recent Issues of NIFS Series

NIFS-277 J. Uramoto,
A Possibility of π^- Meson Production by a Low Energy Electron Bunch and Positive Ion Bunch; Apr. 1994

NIFS-278 K. Itoh, S.-I. Itoh, A. Fukuyama, M. Yagi and M. Azumi,
Self-sustained Turbulence and L-mode Confinement in Toroidal Plasmas II; Apr. 1994

NIFS-279 K. Yamazaki and K.Y.Watanabe,
New Modular Heliotron System Compatible with Closed Helical Divertor and Good Plasma Confinement; Apr. 1994

NIFS-280 S. Okamura, K. Matsuoka, K. Nishimura, K. Tsumori, R. Akiyama, S. Sakakibara, H. Yamada, S. Morita, T. Morisaki,. N. Nakajima, K. Tanaka, J. Xu, K. Ida, H. Iguchi, A. Lazaros, T. Ozaki, H. Arimoto, A. Ejiri, M. Fujiwara, H. Idei. O. Kaneko, K. Kawahata, T. Kawamoto, A. Komori, S. Kubo, O. Motojima, V.D. Pustovitov, C. Takahashi, K. Toi and I. Yamada,
High-Beta Discharges with Neutral Beam Injection in CHS; Apr. 1994

NIFS-281 K. Kamada, H. Kinoshita and H. Takahashi,
Anomalous Heat Evolution of Deuteron Implanted Al on Electron Bombardment ; May 1994

NIFS-282 H. Takamaru, T. Sato, K. Watanabe and R. Horiuchi,
Super Ion Acoustic Double Layer; May 1994

NIFS-283 O.Mitarai and S. Sudo
Ignition Characteristics in D-T Helical Reactors; June 1994

NIFS-284 R. Horiuchi and T. Sato,
Particle Simulation Study of Driven Magnetic Reconnection in a Collisionless Plasma; June 1994

NIFS-285 K.Y. Watanabe, N. Nakajima, M. Okamoto, K. Yamazaki, Y. Nakamura, M. Wakatani,
Effect of Collisionality and Radial Electric Field on Bootstrap Current in LHD (Large Helical Device); June 1994

NIFS-286 H. Sanuki, K. Itoh, J. Todoroki, K. Ida, H. Idei, H. Iguchi and H. Yamada,
Theoretical and Experimental Studies on Electric Field and Confinement in Helical Systems; June 1994

NIFS-287 K. Itoh and S-I. Itoh,
Influence of the Wall Material on the H-mode Performance; June 1994

NIFS-288 K. Itoh, A. Fukuyama, S.-I. Itoh, M. Yagi and M. Azumi
Self-Sustained Magnetic Braiding in Toroidal Plasmas: July 1994

NIFS-289 Y. Nejoh,
Relativistic Effects on Large Amplitude Nonlinear Langmuir Waves in a Two-Fluid Plasma; July 1994

NIFS-290 N. Ohyabu, A. Komori, K. Akaishi, N. Inoue, Y. Kubota, A.I. Livshit, N. Noda, A. Sagara, H. Suzuki, T. Watanabe, O. Motojima, M. Fujiwara, A. Iiyoshi,
Innovative Divertor Concepts for LHD; July 1994

NIFS-291 H. Idei, K. Ida, H. Sanuki, S. Kubo, H. Yamada, H. Iguchi, S. Morita, S. Okamura, R. Akiyama, H. Arimoto, K. Matsuoka, K. Nishimura, K. Ohkubo, C. Takahashi, Y. Takita, K. Toi, K. Tsumori and I. Yamada,
Formation of Positive Radial Electric Field by Electron Cyclotron Heating in Compact Helical System; July 1994

NIFS-292 N. Noda, A. Sagara, H. Yamada, Y. Kubota, N. Inoue, K. Akaishi, O. Motojima, K. Iwamoto, M. Hashiba, I. Fujita, T. Hino, T. Yamashina, K. Okazaki, J. Rice, M. Yamage, H. Toyoda and H. Sugai,
Boronization Study for Application to Large Helical Device; July 1994

NIFS-293 Y. Ueda, T. Tanabe, V. Philipps, L. Könen, A. Pospieszczyk, U. Samm, B. Schweer, B. Unterberg, M. Wada, N. Hawkes and N. Noda,
Effects of Impurities Released from High Z Test Limiter on Plasma Performance in TEXTOR; July. 1994

NIFS-294 K. Akaishi, Y. Kubota, K. Ezaki and O. Motojima,
Experimental Study on Scaling Law of Outgassing Rate with A Pumping Parameter, Aug. 1994

NIFS-295 S. Bazdenkov, T. Sato, R. Horiuchi, K. Watanabe
Magnetic Mirror Effect as a Trigger of Collisionless Magnetic Reconnection, Aug. 1994

NIFS-296 K. Itoh, M. Yagi, S.-I. Itoh, A. Fukuyama, H. Sanuki, M. Azumi
Anomalous Transport Theory for Toroidal Helical Plasmas,
Aug. 1994 (IAEA-CN-60/D-III-3)

NIFS-297 J. Yamamoto, O. Motojima, T. Mito, K. Takahata, N. Yanagi, S. Yamada, H. Chikaraishi, S. Imagawa, A. Iwamoto, H. Kaneko, A. Nishimura, S. Satoh, T. Satow, H. Tamura, S. Yamaguchi, K. Yamazaki, M. Fujiwara, A. Iiyoshi and LHD group,
New Evaluation Method of Superconductor Characteristics for Realizing the Large Helical Device; Aug. 1994 (IAEA-CN-60/F-P-3)

NIFS-298 A. Komori, N. Ohyabu, T. Watanabe, H. Suzuki, A. Sagara, N. Noda,

K. Akaishi, N. Inoue, Y. Kubota, O Motojima, M. Fujiwara and A. Iiyoshi,
Local Island Divertor Concept for LHD; Aug. 1994 (IAEA-CN-60/F-P-4)

NIFS-299 K. Toi, T. Morisaki, S. Sakakibara, A. Ejiri, H. Yamada, S. Morita, K. Tanaka, N. Nakajima, S. Okamura, H. Iguchi, K. Ida, K. Tsumori, S. Ohdachi, K. Nishimura, K. Matsuoka, J. Xu, I. Yamada, T. Minami, K. Narihara, R. Akiyama, A. Ando, H. Arimoto, A. Fujisawa, M. Fujiwara, H. Idei, O. Kaneko, K. Kawahata, A. Komori, S. Kubo, R. Kumazawa, T. Ozaki, A. Sagara, C. Takahashi, Y. Takita and T. Watari
Impact of Rotational-Transform Profile Control on Plasma Confinement and Stability in CHS; Aug. 1994 (IAEA-CN-60/A6/C-P-3)

NIFS-300 H. Sugama and W. Horton,
Dynamical Model of Pressure-Gradient-Driven Turbulence and Shear Flow Generation in L-H Transition; Aug. 1994 (IAEA/CN-60/D-P-I-11)

NIFS-301 Y. Hamada, A. Nishizawa, Y. Kawasumi, K.N. Sato, H. Sakakita, R. Liang, K. Kawahata, A. Ejiri, K. Narihara, K. Sato, T. Seki, K. Toi, K. Itoh, H. Iguchi, A. Fujisawa, K. Adachi, S. Hidekuma, S. Hirokura, K. Ida, M. Kojima, J. Koog, R. Kumazawa, H. Kuramoto, T. Minami, I. Negi, S. Ohdachi, M. Sasao, T. Tsuzuki, J. Xu, I. Yamada, T. Watari,
Study of Turbulence and Plasma Potential in JIPP T-IIU Tokamak;
Aug. 1994 (IAEA/CN-60/A-2-III-5)

NIFS-302 K. Nishimura, R. Kumazawa, T. Mutoh, T. Watari, T. Seki, A. Ando, S. Masuda, F. Shinpo, S. Murakami, S. Okamura, H. Yamada, K. Matsuoka, S. Morita, T. Ozaki, K. Ida, H. Iguchi, I. Yamada, A. Ejiri, H. Idei, S. Muto, K. Tanaka, J. Xu, R. Akiyama, H. Arimoto, M. Isobe, M. Iwase, O. Kaneko, S. Kubo, T. Kawamoto, A. Lazaros, T. Morisaki, S. Sakakibara, Y. Takita, C. Takahashi and K. Tsumori,
ICRF Heating in CHS; Sep. 1994 (IAEA-CN-60/A-6-I-4)

NIFS-303 S. Okamura, K. Matsuoka, K. Nishimura, K. Tsumori, R. Akiyama, S. Sakakibara, H. Yamada, S. Morita, T. Morisaki, N. Nakajima, K. Tanaka, J. Xu, K. Ida, H. Iguchi, A. Lazaros, T. Ozaki, H. Arimoto, A. Ejiri, M. Fujiwara, H. Idei, A. Iiyoshi, O, Kaneko, K. Kawahata, T. Kawamoto, S. Kubo, T. Kuroda, O. Motojima, V.D. Pustovitov, A. Sagara, C. Takahashi, K. Toi and I. Yamada,
High Beta Experiments in CHS; Sep. 1994 (IAEA-CN-60/A-2-IV-3)

NIFS-304 K. Ida, H. Idei, H. Sanuki, K. Itoh, J. Xu, S. Hidekuma, K. Kondo, A. Sahara, H. Zushi, S.-I. Itoh, A. Fukuyama, K. Adati, R. Akiyama, S. Bessho, A. Ejiri, A. Fujisawa, M. Fujiwara, Y. Hamada, S. Hirokura, H. Iguchi, O. Kaneko, K. Kawahata, Y. Kawasumi, M. Kojima, S. Kubo, H. Kuramoto, A. Lazaros, R. Liang, K. Matsuoka, T. Minami, T. Mizuuchi, T. Morisaki, S. Morita, K. Nagasaki, K. Narihara, K. Nishimura, A. Nishizawa, T. Obiki, H. Okada, S. Okamura, T. Ozaki, S. Sakakibara, H. Sakakita, A. Sagara, F. Sano, M. Sasao, K. Sato, K.N. Sato, T. Saeki, S. Sudo, C. Takahashi, K. Tanaka, K. Tsumori, H.Yamada, I. Yamada, Y. Takita, T. Tuzuki, K. Toi and T. Watari,

Control of Radial Electric Field in Torus Plasma; Sep. 1994
(IAEA-CN-60/A-2-IV-2)

NIFS-305 T. Hayashi, T. Sato, N. Nakajima, K. Ichiguchi, P. Merkel, J. Nührenberg, U. Schwenn, H. Gardner, A. Bhattacharjee and C.C.Hegna,
Behavior of Magnetic Islands in 3D MHD Equilibria of Helical Devices;
Sep. 1994 (IAEA-CN-60/D-2-II-4)

NIFS-306 S. Murakami, M. Okamoto, N. Nakajima, K.Y. Watanabe, T. Watari, T. Mutoh, R. Kumazawa and T. Seki,
Monte Carlo Simulation for ICRF Heating in Heliotron/Torsatrons;
Sep. 1994 (IAEA-CN-60/D-P-I-14)

NIFS-307 Y. Takeiri, A. Ando, O. Kaneko, Y. Oka, K. Tsumori, R. Akiyama, E. Asano, T. Kawamoto, T. Kuroda, M. Tanaka and H. Kawakami
Development of an Intense Negative Hydrogen Ion Source with a Wide-Range of External Magnetic Filter Field; Sep. 1994

NIFS-308 T. Hayashi, T. Sato, H.J. Gardner and J.D. Meiss,
Evolution of Magnetic Islands in a Heliac; Sep. 1994

NIFS-309 H. Amo, T. Sato and A. Kageyama,
Intermittent Energy Bursts and Recurrent Topological Change of a Twisting Magnetic Flux Tube; Sep.1994

NIFS-310 T. Yamagishi and H. Sanuki,
Effect of Anomalous Plasma Transport on Radial Electric Field in Torsatron/Heliotron; Sep. 1994

NIFS-311 K. Watanabe, T. Sato and Y. Nakayama,
Current-profile Flattening and Hot Core Shift due to the Nonlinear Development of Resistive Kink Mode; Oct. 1994

NIFS-312 M. Salimullah, B. Dasgupta, K. Watanabe and T. Sato,
Modification and Damping of Alfvén Waves in a Magnetized Dusty Plasma; Oct. 1994

NIFS-313 K. Ida, Y. Miura, S -I. Itoh, J.V. Hofmann, A. Fukuyama, S. Hidekuma, H. Sanuki, H. Idei, H. Yamada, H. Iguchi, K. Itoh,
Physical Mechanism Determining the Radial Electric Field and its Radial Structure in a Toroidal Plasma; Oct. 1994

NIFS-314 Shao-ping Zhu, R. Horiuchi, T. Sato and The Complexity Simulation Group,
Non-Taylor Magnetohydrodynamic Self-Organization; Oct. 1994